

Probing Bulk Superconducting Order Parameter in Ba(K)Fe₂As₂ by Four Complementary Techniques

A. V. Muratov^{1,*}, T. E. Kuzmicheva¹, A. V. Sadakov¹, S. Yu. Gavrilkin¹, D. A. Knyazev^{1,2}, S. A. Kuzmichev^{1,3}, Yu. A. Aleshchenko^{1,4}, A. A. Kordyuk⁵, V. M. Pudalov^{1,6}, and M. Abdel-Hafiez⁷

¹ *P. N. Lebedev Physical Institute, Russian Academy of Sciences, Moscow 119991, Russia*

² *International Laboratory of High Magnetic Fields and Low Temperatures, Wroclaw 253-421, Poland*

³ *Low Temperature Physics and Superconductivity Department, Physics Faculty, M.V. Lomonosov Moscow State University, 119991 Moscow, Russia*

⁴ *National Research Nuclear University MEPhI (Moscow Engineering Physics Institute), Moscow 115409, Russia*

⁵ *Institute of Metal Physics of National Academy of Sciences of Ukraine, 03142 Kyiv, Ukraine*

⁶ *National Research University Higher School of Economics, 101000 Moscow, Russia and*

⁷ *Institute of Physics, Goethe University Frankfurt, 60438 Frankfurt, Germany*

(Dated: February 21, 2017)

Using *four* different experimental techniques, we performed comprehensive studies of the *bulk* superconductive properties of single crystals of the nearly optimally doped Ba_{1-x}K_xFe₂As₂ ($T_c \approx 36$ K), a typical representative of the 122 family. We investigated temperature dependences of the (i) specific heat $C_{el}(T)$, (ii) lower critical magnetic field $H_{c1}(T)$, (iii) intrinsic multiple Andreev reflection effect (IMARE), and (iv) infrared reflectivity spectra. All data clearly show the presence of (at least) two superconducting nodeless gaps. The quantitative data on the superconducting spectrum obtained by four different techniques are consistent with each other: (a) the small superconducting gap $\Delta_S(0) \approx 1.8 - 2.5$ meV, and the large gap energy $\Delta_L(0) \approx 9.5 - 11.3$ meV that demonstrates the signature of an extended *s*-wave symmetry ($\sim 33\%$ in-plane anisotropy), (b) the characteristic ratio $2\Delta_L/k_B T_c$ noticeably exceeds the BCS value.

PACS numbers: 74.25.Bt, 74.25.Dw, 74.25.Jb, 74.70.Dd, 74.45.+c, 74.70.Xa

INTRODUCTION

The symmetry structure of Cooper pairs is thought to be the key to the understanding of the pairing mechanism of their superconductivity. It is well-known that in conventional superconductors the electron-phonon interaction gives rise to the attraction between two electrons, thus forming Cooper pairs. However, Superconductors, whose averaged order parameter over the entire Fermi surface yields zero, are called unconventional. In Iron-based superconductors, the popular opinion is that the electron-phonon is not strong enough to overcome Coulomb repulsion and form Cooper pairs. The nature of the pairing state in iron-based superconductors is the subject of much debate [1–6].

The ternary iron arsenide BaFe₂As₂ shows superconductivity at about 37 – 38 K by hole doping [7]. Among various known Fe-based superconductors (FeBS), these 122 type family compounds may be grown as high quality and large size single crystals with easily variable doping. Band structure calculations show that the low energy bands are dominated by the Fe 3*d* orbitals forming multiple band metallic state: hole-like Fermi surfaces (FS) around the Γ (0,0) point and electron-like Fermi sheets around the M (π, π) point in the Brillouin zone (BZ). The electron and hole-like FS sheets in the normal state of (Ba_{1-x}K_x)Fe₂As₂ observed in angle-resolved photoemission spectroscopy (ARPES) are gapped by either the spin density wave (SDW) [8, 9] or superconducting [10, 11] order in the parent ($x = 0$) or superconducting ($x > 0.15$)

compound, respectively.

It is well experimentally established that potassium doping leads to suppression of the SDW ordering in the parent BaFe₂As₂ compound and induces superconducting (SC) state. The Hall coefficient and thermoelectric power (TEP) measurements for the parent BaFe₂As₂ indicate *n*-type carriers, whereas potassium doping leads to change of the sign in Hall and TEP coefficients, thus indicating *p*-type carriers in superconducting Ba_{1-x}K_xFe₂As₂ [10]. For the optimal doping $x \approx 0.4$ the superconducting critical temperature reaches $T_c \approx 38$ K [7, 12].

In the normal state, the electron and hole sheets of the FS are of a comparable size [13–16]. In the superconducting state, several energy bands at the Fermi energy give rise to multiple energy gaps in the respective superconducting condensates [1]. Recent specific heat, magnetization, muon spin rotation (μ SR), tunneling spectroscopy, Andreev reflection spectroscopy, and ARPES measurements provide clear evidence of multiple gap structures in 122-type FeBS.

The available quantitative experimental data on the key superconducting parameters probed by distinct techniques as well as in various experiments are far of being consistent. Also, identification of the superconducting gaps with the relevant FS bands is hampered by the fact that each particular probe is sensitive only in a limited energy range. Thus far, thermodynamic specific heat measurements with optimally doped BKFA crystals revealed either two nodeless superconducting gaps,

$\Delta_1 = 11\text{ meV}$ and $\Delta_2 = 3.5\text{ meV}$ [12], or one gap: $\Delta = 6\text{ meV}$ [17], or 6.6 meV [18]. By fitting temperature dependence of the lower critical magnetic field $H_{c1}(T)$ extracted from low field magnetization measurements, two superconducting gaps were found in Ref. [19], $\Delta_1(0) = 8.9 \pm 0.4\text{ meV}$, and $\Delta_2(0) = 2.0 \pm 0.3\text{ meV}$. Penetration depth extracted from μSR leads to $\Delta_1 = 9.1\text{ meV}$, and $\Delta_2 = 1.5\text{ meV}$ [20].

The specific heat (SH) measurements [12, 21, 22] are known to suffer of several evident problems with data treatment. The SH data contains contribution from the lattice, that is subtracted to some extent in order to determine the electronic contribution. The lattice contribution to the SH is typically estimated by suppressing the SC transition in high magnetic fields or by measuring SH for the parent non-SC compound. Therefore, the lattice SH cannot be accurately obtained in FeBS because of the very high upper critical field and because of magnetic/structural phase transitions at higher temperature in the parent compound. The majority of the earlier SH data suffer from a residual low-temperature non-superconducting electronic contribution and show Schottky anomalies [22, 23]. Moreover, superconductivity-induced electronic SH is very sensitive to the sample quality and phase purity [12]. Also, in the earlier SH data analysis, the data are commonly fitted to the phenomenological multiband α -model [24, 25], that assumes a BCS temperature dependence of the gaps. However, our direct measurements by means of multiple Andreev reflections effect (MARE) spectroscopy [26–31] do not support this assumption and clearly show that the $\Delta(T)$ dependences for the multiband superconductors (such as MgB_2 , and FeBS) deviate from the BCS-type because of the interband coupling. Finally, fitting the SH data with the multiband model requires several adjustable parameters.

The amount of the SC gaps detected in ARPES measurements varies, depending, apparently, on the instrument resolution, crystal and its surface quality: initial experiments [15] reported large gap $\Delta_1 = 12\text{ meV}$ on both small hole-like and electron-like FS sheets, and a small gap $\Delta_2 = 6\text{ meV}$ on the large hole-like FS; similar results were reported in Ref. [20]: $\Delta_1 = 9.1\text{ meV}$, and $\Delta_2 < 4\text{ meV}$. It should be noted that the small gaps developed on the inner hole and inner electron FS are difficult to resolve experimentally in ARPES measurements. Later, some more SC nodeless gaps were observed; particularly, in Ref. [32] the inner FS sheet around Γ point was found to show large ($10 - 12\text{ meV}$) and slightly momentum-dependent gap while the outer FS sheet has nearly isotropic small gap ($7 - 8\text{ meV}$). In Ref. [16] three hole condensates (α, β, γ) were found around Γ point, and one electron condensate (η) around M-point of the BZ, all with nodeless SC gaps. Δ_α was found warped along k_z : $\Delta_\alpha = 6 - 11.5\text{ meV}$ as $11.5 \cos(k_x a) \cos(k_y b) + 2.1 \cos(k_z c)$, whereas Δ_β and Δ_γ

were isotropic. The η SC-gap is also almost isotropic along z and a rhomb-like anisotropic in the ab -plane. Finally, in STS tunneling measurements two nodeless gaps $\Delta_2 = 7.6$, and $\Delta_1 = 3.3\text{ meV}$ were found in Ref. [33].

Substantial efforts have been made in order to understand the physics of the pairing mechanism. On the theory side, for the Fe-based superconductors, which have both electron-like and hole-like pockets, there is general agreement among theoretical approaches [34–39] that the starting point to the gap symmetry is the s^\pm type with opposite sign of the gap on the electron and hole pockets. This symmetry, however, may change as FS sheets size changes [10, 40], or as nonmagnetic impurities are introduced [41]. The majority of experimental data, cited above reported nodeless s -type symmetry gaps. However, thermodynamic probes are sensitive to the line nodes with sufficiently high spectral weight, whose existence in BKFA they rule out. ARPES measurements with optimally doped $(\text{Ba}_{1-x}\text{K}_x)\text{Fe}_2\text{As}_2$ [15, 34, 42] and $\text{Ba}(\text{Fe}_{1-x}\text{Co}_x)_2\text{As}_2$ [43], have identified nodeless gaps on the hole pockets. We recall that thermodynamic measurements on these same materials [20, 44–46] also show nodeless behavior consistent with s -wave gap symmetry. Recent data of the T_c dependence on nonmagnetic impurities in $\text{Ba}(\text{Fe}_{1-x}\text{Co}_x)_2\text{As}_2$ disordered films [47] initially seemed to be inconsistent with s^\pm type theory predictions [39], however, a more detailed subsequent analysis of the same data [48] lead the authors to the conclusion on the s_\pm gap symmetry. Finally, the phase sensitive SIS tunneling measurements [49] reported the s^\pm symmetry for current injected in the ab -plane (and s^{++} -wave – for current injected along c).

We conclude that the existing experimental data on the gap structure and anisotropy in k -space are contradictory enough. In this context, it is highly important to probe the superconducting properties with a set of independent experimental techniques. Each of the experimental probes has its own limits of applicability and requires particular model assumptions for extracting the quantitative data from the observables. Comparing the results obtained by several independent techniques one may test the validity of model assumption and obtain most reliable information. In Ref. [46] this approach has been implemented by applying two independent bulk probes, i.e. by measuring the London penetration depth and MARE. Despite the fact that well consistent data have been obtained in Ref. [46] on the gap magnitude, these measurements did not fully address the problem since were performed with similar, though not identical samples and even of the nominally different composition, $\text{Ca}_{0.32}\text{Na}_{0.68}\text{Fe}_2\text{As}_2$ and $\text{Ba}_{0.65}\text{K}_{0.35}\text{Fe}_2\text{As}_2$.

This drawback is improved in the current study, where we have succeeded in performing *four* types of measurements with one and the same large size single crystal of nearly optimally doped $(\text{Ba}_{1-x}\text{K}_x)\text{Fe}_2\text{As}_2$ (with $x = 0.33 - 0.35$). In particular, we have measured tem-

perature dependences of the specific heat, lower critical field, H_{c1} , multiple Andreev reflections effect, and infrared reflectance spectra. We obtained self-consistent data that clearly shows the presence of two or more superconducting condensates with nodeless order parameters. The quantitative data on the superconducting properties obtained by four complementary techniques may be summarized as follows: (a) the superconducting state has two (or more) nodeless gaps: the large gap, $\Delta_L = 9.5 - 11.3$ meV with extended s -wave symmetry, and the small gap, $\Delta_S = 1.8 - 2.5$ meV; (b) both energy gaps fall with temperature in the way different from the single-band BCS-like behavior, (c) the characteristic ratio $2\Delta_L/k_B T_C$ noticeably exceeds the BCS limit and indicates rather strong electron-boson coupling in the driving bands.

EXPERIMENTAL DETAILS

The large size single crystal of $\text{Ba}_{1-x}\text{K}_x\text{Fe}_2\text{As}_2$ was synthesized by self-flux technique using FeAs as the flux, for details see [50, 51]. For Ba-122 FeBS, optimal level corresponds to $x \approx 0.4$ for K doping ($T_c = 38.5$ K) [12, 52].

The chemical composition of our sample was verified by energy dispersive X-ray (EDX) spectroscopy probe. According to the magnetic susceptibility measurements in zero field (see upper inset of Fig. 1) and specific heat measurements the critical temperature of the superconducting transition $T_c = 36.5 \pm 0.2$ K. If one relies on the known phase diagram [52] the average bulk doping level of the studied samples may be concluded to correspond to $x = 0.33$.

The high quality of the crystals is confirmed by various physical characterizations: (i) a sharp superconducting transition observed in susceptibility and specific heat measurements at $T \approx 37$ K [21] (see inset of Fig.1) confirming the good quality of the single crystal [21]; (ii) the chemical composition, crystal structure and lattice parameters tested by X-ray diffraction (Pan Analytical X'Pert Pro MRD). The critical temperature $T_c \approx 36.5$ – 37 K, is evidenced by magnetization, DC transport measurements, and also by Andreev reflection spectra flattening measured at various points of the bulk crystal.

Low field magnetization measurements were performed by using a SQUID magnetometer MPMS-XL7, and specific heat measurements - with PPMS-9 system, both from Quantum Design. Infrared reflectance (IR) spectra were measured with IFS-125HR Fourier transform infrared spectrometer from Bruker, and Andreev reflection spectra were obtained by the break-junction technique [30, 53].

DC MAGNETIZATION

The London penetration depth λ is a fundamental parameter that carries signatures of the pairing mechanism, and therefore is a powerful tool for probing the superconducting state [54]. The London penetration depth is related to lower critical field H_{c1} , that pinpoints the vortices penetration into the sample.

In this section we report measurements of the first critical field H_{c1} for $\text{Ba}_{1-x}\text{K}_x\text{Fe}_2\text{As}_2$ sample. Our analysis of temperature dependence of the lower critical field $H_{c1}(T)$ for the $B||c$ direction support the presence of two s -wave-like gaps with strongly different magnitudes and slightly different contributions. By analyzing the H_{c1} temperature dependence we reveal the presence of the two SC condensates with s -type symmetry of the order parameter. The two SC gap values extracted from the $H_{c1}(T)$ analysis correspond to $2\Delta_1(0)/k_B T_c = 1.2 \pm 0.2$ (or $\Delta_1(0) = 2 \pm 0.3$ meV), and $2\Delta_2(0)/k_B T_c = 6.9 \pm 0.3$ (or $\Delta_2(0) = 11 \pm 0.5$ meV); their weights extracted by fitting with the α -model are $\varphi_1 = 0.54 \pm 0.02$ for the small gap and $\varphi_2 = 0.46 \pm 0.02$ for the large gap.

Experimental

The DC magnetization measurements were performed with a rectangular slab, $3 \times 4 \times 0.05$ mm³, cleft from the same large crystal used for all other measurements.

The approach used for extracting the first critical magnetic field is based on measuring the magnetic field value, for which the vortexes start penetrating into superconducting bulk destroying the ideal Meissner effect. In other words, we determined such field value H_{c1} which corresponds to the onset of nonlinear M versus H dependence. Measurements were performed with MPMS-XL7 (Quantum Design) in the temperature range 2–36 K with a step size of 1 K. Magnetic field direction was aligned with the crystal c -axis.

Results

At first step we checked pinning properties by measuring of magnetic hysteresis loops at several temperatures (lower inset to Fig. 1). Magnetization curve $M(H)$ is symmetric about the axis $M=0$ that indicates a strong bulk pinning and the absence of Bean-Levingston barrier. Also $M(H)$ shows no magnetic background.

The raw experimental data for $M(H)$ dependences in low fields are presented in Fig. 1. In fields above H_{c1} the superconductor captures magnetic flux, that leads to departure of $M(H)$ dependence from the linear one. Exact finding of the H_{c1} values from the measured nonlinear $M(H)$ dependence is a hard task, taking into account a finite width of the linear-to-nonlinear

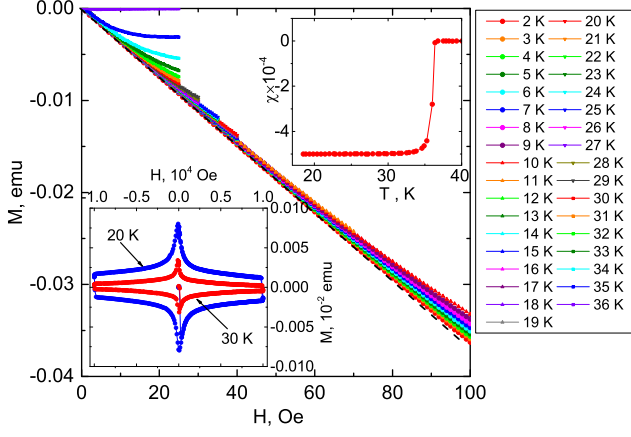


FIG. 1: Magnetic field dependence of the magnetization in the temperature range 2–36 K. The dashed straight line extrapolates the linear $M(H)$ dependence observed in weak fields. Upper inset shows magnetic susceptibility of the $\text{Ba}_{0.67}\text{K}_{0.33}\text{Fe}_2\text{As}_2$ sample, measured in zero field. Lower inset: magnetization hysteresis loops measured at 20 and 30 K.

crossover of the magnetization curves, and data scattering. In our measurements the noise level corresponded to $\approx (3-5) \times 10^{-5}$ emu. By modeling the $M(H)$ dependence with such noise level we found that the frequently used algorithm for the H_{c1} determination based on the correlation parameter, (see e.g., [46, 55]) leads to artificially overestimated H_{c1} data and excessive $H_{c1}(T)$ data scattering.

Correspondingly, instead of the above algorithm [46] based on regression calculation, we have developed a modified algorithm where the experimental $M(H)$ data are fitted with both, linear (for $H < H_{c1}$) and the second power polynomials (for $H > H_{c1}$). The protocol of Refs. [46, 55] and its shortcomings in the case of a large noise level, as well as the modified algorithm are described in detail in Appendix 1. This approach minimizes the impact of a variable number of points on the correlation coefficient calculation and thus improves the accuracy of the H_{c1} determination. The $H_{c1}(M)$ dependence determined with the modified algorithm for the studied BKFA sample is shown in Fig. 2

It should be mentioned that the determined H_{c1} value represents a critical field for the given sample. In order to characterize the material parameter, one has also to take the demagnetization factor N into account:

$$H_{c1} = \frac{H_{c1}^{\text{measured}}}{1 - N}, \quad (1)$$

where

$$N = \frac{q \frac{a}{b}}{q \frac{a}{b} + 1}. \quad (2)$$

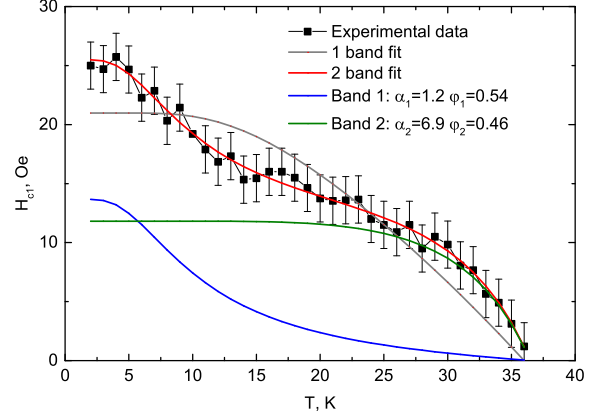


FIG. 2: H_{c1} temperature dependence for the BKFA sample compared with the single band BCS model and the two band α -model

For the disk-shape sample [56]:

$$q_{\text{disk}} = \frac{4}{3\pi} + \frac{2}{3\pi} \tanh \left[1.27 \frac{b}{a} \left(\ln \left(1 + \frac{a}{b} \right) \right) \right]. \quad (3)$$

With the sample diameter $a = 3 \pm 0.5$ mm and thickness $b = 50 \pm 20$ μm the demagnetization factor for our sample $N = 0.96 \pm 0.02$, and the ratio of the material H_{c1} and the measured H_{c1} value amounts to $\sim 16-50$. Correspondingly, the H_{c1} value for $\text{Ba}_{0.67}\text{K}_{0.33}\text{Fe}_2\text{As}_2$ falls into a range of fields 400 – 1250 Oe.

For describing the lower critical field of a superconductor, it is convenient to introduce a normalized superfluid density [19]:

$$\tilde{\rho}_s(T) \equiv \lambda(0)_{ab}^2 / \lambda(T)_{ab}^2 = H_{c1}(T) / H_{c1}(0). \quad (4)$$

In the framework of the BCS theory for a single-band superconductor with an isotropic gap, the latter may be represented as [57, 58]:

$$\tilde{\rho}_s(T) = 1 + 2 \int_{\Delta(T)}^{\infty} \frac{\partial f}{\partial E} \frac{E dE}{\sqrt{E^2 - \Delta^2(T)}}. \quad (5)$$

Here $f(T)$ is the Fermi distribution function, $\Delta(T) = \Delta_0 \tanh \left[1.82 \left(1.018 \left(\frac{T_c}{T} - 1 \right) \right)^{0.51} \right]$ is the gap temperature dependence. $E^2 = \varepsilon^2 + \Delta^2(T)$, E is the total energy, and ε - single particle excitation energy counted from the Fermi energy. The normalized superfluid density may be re-written in a more convenient for integration way as follows:

$$\tilde{\rho}_s(T) = 1 - 2 \int_0^{\infty} \frac{e^y}{(e^y + 1)^2} \frac{1}{t} d\xi, \quad (6)$$

with $t = T/T_c$, $y = \sqrt{\xi^2 + \left(\frac{\alpha \delta(T)}{2} \right)^2} / t$, $\xi = \varepsilon / (k_B T_c)$, and $\alpha = 2\Delta_0 / (k_B T_c)$. The latter is the parameter in the given model.

Figure 2 shows the least square fitting of the measured $H_{c1}(T)$ data within the above single-band BCS model. The fitting parameter here $\alpha = 3.4$. One can see that the model fails to reproduce the experimental data. Clearly, the single band model can not describe the curved $H_{c1}(T)$ dependence, especially in the interval 10 – 25 K. The physical meaning of this failure is transparent: to fit the data successfully one needs to use a multiband model.

Correspondingly, at the next step for describing the experimental data we apply the so called two-band α -model [57]:

$$\tilde{\rho}_s(T) = \varphi_1 \tilde{\rho}_{s1}(T) + \varphi_2 \tilde{\rho}_{s2}(T) \quad (7)$$

This model considers a normalized superfluid density for the superconductor having two independent condensates with a normalized superfluid densities ρ_{s1} and ρ_{s2} in the first and second band respectively, taken with weighting factors φ_1 and $\varphi_2 = 1 - \varphi_1$.

The result of fitting the $H_{c1}(T)$ data with α model is shown in Fig. 2. This approach leads to a good agreement between the model and experimental data. The fitting parameters are as follows: $\alpha_1 = 1.2 \pm 0.2$ ($\Delta_1(0) = 2 \pm 0.3$ meV), weight factor $\varphi_1 = 0.54 \pm 0.02$; and $\alpha_2 = 6.9 \pm 0.3$ ($\Delta_2(0) = 11 \pm 0.5$ meV), weight factor $\varphi_2 = 0.46 \pm 0.02$; $H_{c1}(0) = 25.5$ Oe.

SPECIFIC HEAT

The specific heat measurements are a powerful thermodynamic bulk probe [12, 21, 22], though there are several known problems with SH data treatment. The SH data contains contribution from the lattice, that is to be subtracted in order to determine the electronic SH. The lattice contribution to the SH is usually estimated by suppressing the superconducting transition in high magnetic fields. For FeBS, the lattice SH cannot be suppressed because of the very high upper critical field. The majority of the earlier SH data suffer from a residual low-temperature non-superconducting electronic contribution and show a Schottky anomaly [22, 23].

In this section we report our SH data and their analysis which evidence for the two-band superconducting condensate with s -type order parameter symmetry. The extracted superconducting gap values correspond to the characteristic ratios $2\Delta_1(0)/k_B T_c = 1.6 \pm 0.1$ ($\Delta_1(0) = 2.5 \pm 0.2$ meV, weight factor $\varphi_1 = 0.58 \pm 0.02$) and $2\Delta_2(0)/k_B T_c = 7.2 \pm 0.2$ ($\Delta_2(0) = 11.3 \pm 0.3$ meV, weighting factor $\varphi_2 = 0.42 \pm 0.02$). These parameters are consistent with those determined from magnetization measurements, IR reflection, and Andreev reflection spectra, described in the corresponding sections.

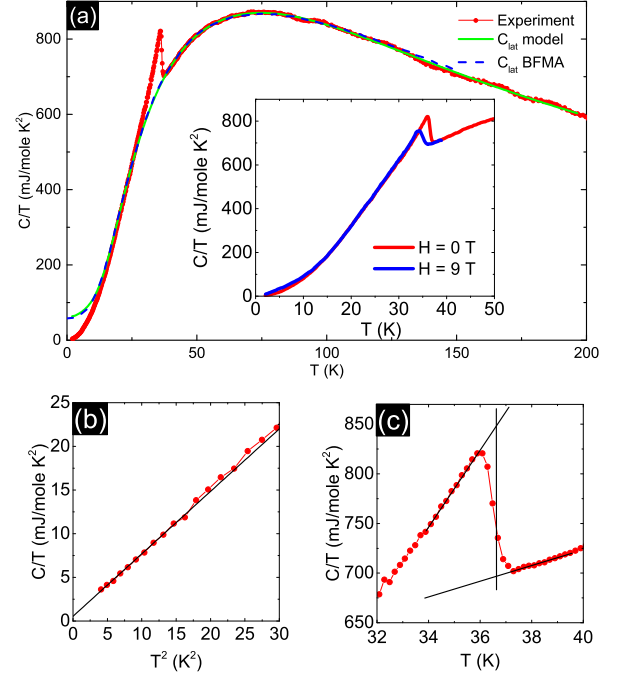


FIG. 3: (a) Temperature dependence of the specific heat for $\text{Ba}_{0.67}\text{K}_{0.33}\text{Fe}_2\text{As}_2$ sample, normalized by temperature at zero field and comparison with two models, using the common states approximation: for the 6-modes Einstein model and for the lattice SH of $\text{Ba}(\text{Fe}_{0.88}\text{Mn}_{0.12})_2\text{As}_2$. Insert compares the data for $B = 0$ and $B = 9$ T. (b) Low-temperature behavior of the normalized specific heat versus T^2 . Dots are the experimental data, black curve – their fit with the Debye law. For quantitative extraction of the parameters we used only the data in the range 2 – 4 K. (c) SH anomaly at the superconducting transition and determination of T_c .

Experimental

The specific heat measurements were taken with a 1.93 mg-piece of $\text{Ba}_{1-x}\text{K}_x\text{Fe}_2\text{As}_2$ ($x = 0.33$) single crystal cleft from the same large crystal that was used for all other measurements; the sample had superconducting critical temperature $T_c = 36.5$ K. Measurements were done using the thermal relaxation technique with PPMS-9, in the temperature range 2 – 200 K. Temperature was swept with a stepsize of 0.2 K for the interval 2 - 50 K, 0.5 K for 50 - 100 K and 1 K for 100 - 200 K. For each temperature point the data have been averaged within 3 seconds.

Results

The raw experimental SH data are shown in Fig. 3 at zero field; the insert shows results obtained with another

piece of the same crystal ($m=0.8\text{ mg}$) in fields $B = 0T$ and $9T$.

The $C(T)/T$ data shows no features in the low temperature range (such as, *e.g.*, growth towards the lowest T), thus evidencing for the absence of Schottky anomaly. In the low- T limit (for $T < 6 - 8\text{ K}$) the $C(T)/T$ data may be represented by the Debye law: $C(T)/T = \gamma(0) + \beta T^2$, where $\gamma(0)$ is the residual contribution of the non-superconducting phase, βT^2 - is the lattice contribution. The two parameters $\gamma(0)$ and β may be easily found from fitting the model to the experimental data (see Fig. 3b). For $B = 0$ we found $\gamma = 0.3 - 0.5\text{ mJ/mol K}^2$ and $\beta = 0.74 - 0.71\text{ mJ/mol K}^4$. The negligibly low value of the residual electronic specific heat evidences for high quality of the sample. It is worth noting that the above approach is rather approximate because beyond the linear approximation the electronic SH for superconducting materials depends on temperature, and because the lattice contribution includes higher order terms. For this reason this approach is appropriate only for qualitative estimates, whereas for quantitative analysis more complex approach is needed, which is described below.

In the temperature interval 36-37K the $C(T)$ data shows a sharp peak, related with the SC transition (see Fig. 3). The peak width is about 1K, and the jump in the C/T data at the transition $\Delta C/T = 119\text{ mJ/mol K}^2$. Due to the entropy conservation at the SC transition, the following equality must be fulfilled:

$$\int_{T_c-t}^{T_c+t} \frac{C_{exp}}{T} dT = \int_{T_c-t}^{T_c} \frac{C_{extrap}}{T} dT + \int_{T_c}^{T_c+t} \frac{C_{extrap}}{T} dT, \quad (8)$$

where C_{exp} - the measured SH data, C_{extrap} - the data extrapolated to the region of the SC transition, and $2t$ is the superconducting transition width. By implementing this implicit equation to the data in Fig. 3c we determine the true T_c value of 36.5K, nicely consistent with that extracted from magnetic measurements.

Separation of the lattice and electronic contributions to SH

Further experimental investigations of the structure and magnitude of the SC gaps by means of bulk specific heat data are of great interest. In order to determine the specific heat related to the SC phase transition, we need to estimate the phonon (lattice) and electronic contributions to specific heat in the normal state. These contributions are additive:

$$C_p(T) = C_e(T) + C_{lat}(T), \quad (9)$$

where C_e is the contribution related to electronic subsystem, and C_{lat} is the lattice contribution. The lattice term C_{lat} however cannot be determined by direct measurements. This problem may be solved by using

the so called common states approximation [59], that consists in using, as a reference, of the lattice SH for a non-superconducting compound of a relative's composition. For $\text{Ba}_{0.67}\text{K}_{0.33}\text{Fe}_2\text{As}_2$ one of such compounds is the parent BaFe_2As_2 that is non-superconducting though exhibits a magnetic phase transition at $\approx 140\text{ K}$. Varying doping level or doping element leads to changes in the lattice spacings by a few percents. In order to take account of these insignificant change one can use scaling factors proximate to unity. Other possible reference materials for our $\text{Ba}_{0.67}\text{K}_{0.33}\text{Fe}_2\text{As}_2$ sample are the non-superconducting compounds $\text{Ba}(\text{Fe}_{0.85}\text{Co}_{0.15})_2\text{As}_2$ [60], $\text{Ba}(\text{Fe}_{0.88}\text{Mn}_{0.12})_2\text{As}_2$ [12], and $\text{BaFe}_{1.75}\text{Ni}_{0.25}\text{As}_2$ [61].

Mathematically, the common states approximation for the specific heat may be written as follows:

$$C_{\text{tot}}^{SC}(T) = C_{el}^{SC}(T) + AC_{\text{lat}}^{nSC}(BT). \quad (10)$$

Here $C_{\text{tot}}^{SC}(T)$ is the total calculated SH corresponding to the experimental data $C_{\text{exp}}(T)$, $C_{el}^{SC}(T)$ is the electronic contribution to SH, $C_{\text{lat}}^{nSC}(T)$ - lattice SH for the nonmagnetic reference compound, A and B are the scaling factors. For temperatures above T_c the electronic SH may be written as $C_{el}^{SC}(T) = \gamma_n T$. The factors A and B are selected based on least square fitting under the constraint of the entropy conservation:

$$\int_0^{T_c} \frac{C_{el}(T)}{T} dT = \int_0^{T_c} \gamma_n dT. \quad (11)$$

By now, the lattice specific heat for $\text{Ba}_{0.68}\text{K}_{0.32}\text{Fe}_2\text{As}_2$ was well described using the Debye-Einstein model [62]. In order to test whether or not we can apply the data of Refs. [12, 61, 62] to the data processing for our $\text{Ba}_{0.67}\text{K}_{0.33}\text{Fe}_2\text{As}_2$ sample, we have tested the results of Ref. [12, 61, 62] for the lattice SH of non-superconducting and non-magnetic materials, and found that these data may be scaled to each other by using the common state approximation with factors A and B chosen rather close to unity, $0.95 - 1.05$.

Correspondingly, for the analysis of our experimental data we used the model described in Ref. [62] containing 6 Einstein modes. We also used the lattice SH data for $\text{Ba}(\text{Fe}_{0.88}\text{Mn}_{0.12})_2\text{As}_2$ [12], since these measurements were done in the most wide temperature range. Figure 3a shows that both models describe the experimental $C(T)$ data rather well. The resulting electronic SH contribution C_{el}/T obtained in this fit using the common state approximation is shown on Fig. 4a, the inset to Fig. 4b demonstrates the entropy conservation constraint for this calculations. In the two respective fittings we obtained the two sets of factors: (i) $A = 0.998$, $B = 0.974$ and $\gamma_n = 63.6\text{ mJ/mol K}^2$ for the 1st scaling based on the lattice SH of $\text{Ba}_{0.68}\text{K}_{0.32}\text{Fe}_2\text{As}_2$, and (ii) $A = 0.954$, $B = 0.996$, $\gamma_n = 58.0\text{ mJ/mol}^2$ for the 2nd scaling based on the lattice SH of $\text{Ba}(\text{Fe}_{0.88}\text{Mn}_{0.12})_2\text{As}_2$.

In order to improve the accuracy of the data analysis we extrapolated the $C_{el}(T)$ data to $T = 0$ for

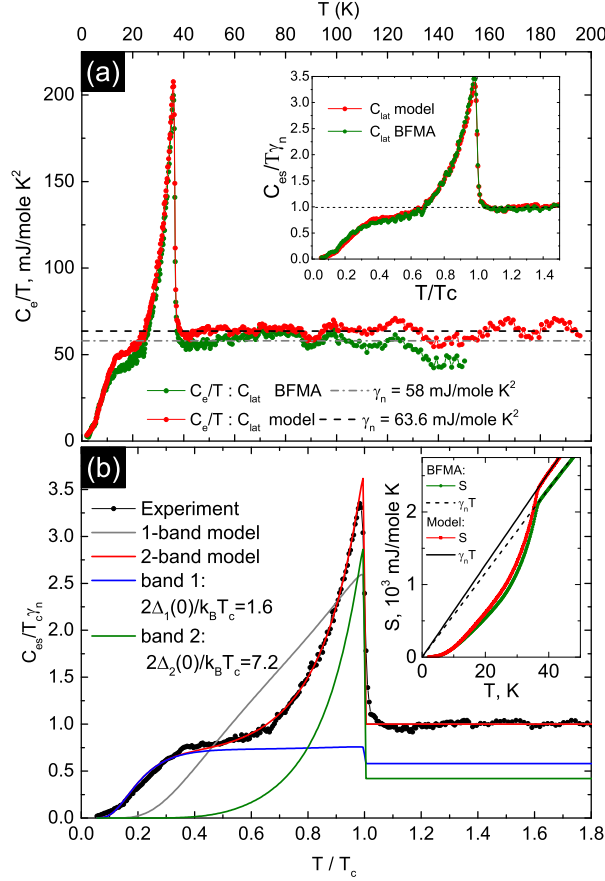


FIG. 4: (a) Electronic SH calculated using the 6-mode Einstein model [62] and the lattice SH of Ba(Fe_{0.88}Mn_{0.12})₂As₂ [12]. Inset: comparison of the normalized electronic SH defined by the 6-mode Einstein model and the lattice SH of Ba(Fe_{0.88}Mn_{0.12})₂As₂; (b) Normalized electronic SH of the superconducting condensate $C_{es}/T\gamma_n$ compared with the single band BCS model and the two band BCS α -model. Inset: Electronic entropy in normal and SC state in case of calculations with 6-mode Einstein model and the lattice SH of Ba(Fe_{0.88}Mn_{0.12})₂As₂.

both models. From this extrapolation we obtained also the two estimates for normal state residual contribution, $\gamma_r = 2.3 \text{ mJ/mol K}^2$ - in the analysis based on the lattice model [62] and $\gamma_r = 1.1 \text{ mJ/mol K}^2$ in the scaling based on the Ba(Fe_{0.88}Mn_{0.12})₂As₂ lattice. We conclude that the non-superconducting residual contribution to SH is of the order of 2 – 4% ($\gamma_r/\gamma_n = 0.019 - 0.035$), that is comparable to the values reported for other superconducting FeBS [60].

Analyzing behavior of the superconducting condensate it is appropriate to consider the normalized electronic SH $C_{es}/T\gamma_n$ versus normalized temperature (T/T_c), where C_{es} is the SH of superconducting condensate [60], which

may be obtained as:

$$\frac{C_{es}}{\gamma_n T}(T) = \frac{C_e/T - \gamma_r}{\gamma_n - \gamma_r} \quad (12)$$

In Fig. 4a, the C_e/T data obtained by two approaches is consistent with each other. Although there is a minor difference (much less than the peak height at T_c) between them in Fig. 4a, the difference becomes almost invisible on the plot of the normalized SH of the superconducting condensate C_{es} , Fig. 4b. For high temperatures, $T > 100 \text{ K}$, the data description based on the Ba(Fe_{0.88}Mn_{0.12})₂As₂ lattice SH is somewhat worse: the difference between C_e/T and γ_n increases with temperature.

Analysis of the normalized electronic SH

The normalized SH of the superconducting condensate may be calculated within the BCS theory as follows [25]:

$$\begin{aligned} \frac{C(T)}{\gamma_n T} &= \frac{d(S/\gamma_n T_c)}{dt}, \\ \frac{S(T)}{\gamma_n T_c} &= \frac{6}{\pi^2} \int_0^\infty [f \ln f + (1-f) \ln(1-f)] d\varepsilon, \\ f &= \left[\exp \frac{(e^2 + \alpha^2 \delta^2(t)/4)^{1/2}}{t} + 1 \right]^{-1}, \\ \delta(T) &= \tanh \left[1.82 \left(1.018 \left(\frac{T}{T_c} - 1 \right) \right)^{0.51} \right]. \end{aligned} \quad (13)$$

where $t = T/T_c$, $\alpha = 2\Delta(0)/k_B T_c$, $\delta(T) = \Delta(T)/\Delta(0)$ is the temperature dependence of the gap, and $\Delta(0)$ is the energy gap at $T = 0$. The above phenomenological formulae [46] generalizes calculations of [63] within the BCS model.

At the first step, for fitting the $C_{es}(T)$ data we applied the single-band BCS model using Eqs. 13. The model implies an isotropic s -type order parameter Δ . Figure 4b shows the result of the mean square fitting with $2\Delta/k_B T_c = 3.7$. Obviously, the single-band approach does not fit the experimental SH data and, particularly, does not reproduce the remarkable hump in $C_{es}/T\gamma_n$ clearly seen at $T/T_c \sim 0.3 - 0.5$.

At the second step we apply the phenomenological α -model [24, 25] for the two-band superconductor, which sums up contributions of each band, calculated within the BCS model, Eq. 13, with the corresponding weight factors φ_1 and $\varphi_2 = 1 - \varphi_1$:

$$C(T) = \varphi_1 C_1(T) + \varphi_2 C_2(T) \quad (14)$$

This model has three adjustable parameters, $\alpha_1 = 2\Delta_1/k_B T_c$, $\alpha_2 = 2\Delta_2/k_B T_c$ and φ_1 , which may be found from least square fitting of the model to the experimental data. φ_1 and φ_2 describe the relative share of each

condensate in the total SH: $\varphi_i = \gamma_i/\gamma_n$, where γ_i is the specific heat of the i -th condensate in the normal state. The result of data fitting with the two-band model is shown in Fig. 4 b.

One can see that the two-band approach provides rather good fitting to the experimental data. The difference between the model dependence and the experimental data does not exceed 5% of $C_{es}/T\gamma_n$, that corresponds to 4 mJ/molK². The deviation is within the measurements uncertainty and in relative units does not exceed 1% of the total measured C_{exp} . With the two band model we find the following set of parameters: $\alpha_1 = 2\Delta_1/k_B T_c = 1.6 \pm 0.1$ ($\Delta_1 = 2.5 \pm 0.2$ meV), $\alpha_2 = 2\Delta_2/k_B T_c = 7.2 \pm 0.2$ ($\Delta_2 = 11.3 \pm 0.3$ meV), and $\varphi_1 = 0.58 \pm 0.02$.

INFRARED REFLECTION SPECTROSCOPY

Infrared (IR) spectroscopy is a powerful technique to investigate the electronic gap structure of superconductors. Its large probe depth ensures the bulk nature of the measured quantities and its high-energy resolution and powerful sum rules enable a reliable determination of important physical parameters, such as the gap magnitude and the plasma frequency of the SC condensate [64]. In a simple one-band system, the standard Drude model with parameters plasma frequency Ω and scattering rate γ describes the frequency-dependent complex conductivity $\tilde{\sigma}_N$ in the normal (N) state [65]. In the superconducting (S) state, the standard BCS model (Mattis-Bardeen equations [66], with parameters σ_0 and superconducting gap Δ) can describe the complex conductivity $\tilde{\sigma}_S$ [67]. On this basis, far-infrared measurements can be of particular importance since a signature of the superconducting gap Δ can be observed at $\hbar\omega \sim 2\Delta$ (optical gap) for an anisotropic s -wave BCS superconductor. The electromagnetic radiation below the gap energy 2Δ could not be absorbed. For a bulk sample, in particular, a maximum at the optical gap is expected in the ratio R_S/R_N , where R_S and R_N are the frequency-dependent reflectances in the superconducting and normal state, respectively [67].

Experimental

IR reflectance spectra $R(\omega)$ were measured with Bruker IFS 125HR spectrometer with a spectral resolution of 2 cm⁻¹ over a wave number range of 400-50 cm⁻¹ (25-200 μ m). For measurements in FIR region we used a mylar beam splitters of various thickness. Liquid-helium cooled Si bolometer was used to detect IR spectra. For low-temperature measurements the sample was placed into the helium cryostat Optistat CF-V from Oxford Instruments with the wedged windows made of TPX

plastic. The reflectance measurements were carried out at near-normal incidence on the freshly cleaved surfaces.

The goal of IR measurements is to determine the frequency-dependent complex conductivity $\tilde{\sigma}(\omega) = \sigma_1(\omega) + i\sigma_2(\omega)$ which usually appears in discussion of the low-frequency electrodynamics of the system [64] and can describe its optical response. The complex conductivity of the ideal single-band conducting system can be described using the Drude model in the normal state and the Bardeen-Mattis BCS model [66] generalized for an isotropic s -wave BCS superconductor using the Zimmermann relations [68]. In this case, in the dirty limit the dissipative part of the optical conductivity $\sigma_1(\omega)$ at $T \ll T_c$ vanishes abruptly below a frequency corresponding to doubled superconducting gap 2Δ . Thus, in the vicinity of the frequency corresponding to 2Δ (optical gap) one should observe a peculiarity in the optical response of the system.

The relatively small size of the sample for IR measurements and irregular cleavage surface resulted in rather low accuracy of measurement of the absolute value of reflection coefficient; the latter hampered calculating the optical conductivity by using the Kramers-Kronig analysis. For this reason we apply the technique described in [69] to determine the superconducting gaps. It consists in the relative measurements of $R(T \ll T_c)/R_N$ with no reference measurements, while sweeping the temperature within a narrow temperature range. Here, R_N is the reflectance in the normal state at temperature slightly above T_c . The measurements are performed in one cycle with the same detector and set of optical elements (beam splitter and cryostat windows). In this way the sample position and orientation as well as the optical system were not changed during measurements. This technique enables to minimize possible temperature-driven distortions of the optical set-up, which may yield frequency-dependent systematic errors in $R(\omega)$. It should be noted that for the bulk superconductor of the s -type symmetry the normalized reflectivity $R(T \ll T_c)/R_N$ forms a maximum, whose energy corresponds to the superconducting gap 2Δ . For the two gap superconductor, the maximum is expected to appear between the two SC gaps, closer to the one having a major contribution. This enables one to estimate the value of the dominant gap.

Results

Figure 5 shows the $R(T)/R(T = 40 \text{ K})$ dependences for Ba_{0.67}K_{0.33}Fe₂As₂ measured at $T = 5 - 50 \text{ K}$. One can see that the normalized reflectivity $R(T)/R(40 \text{ K})$ maximum starts increasing as temperature T decreases below T_c . This is because for s -wave superconductor at temperatures below T_c the reflectance approaches unity at energies $\hbar\omega < 2\Delta$. As a result, a peak is formed with a maximum in the range of $\sim 160 \text{ cm}^{-1}$ (19.8 meV).

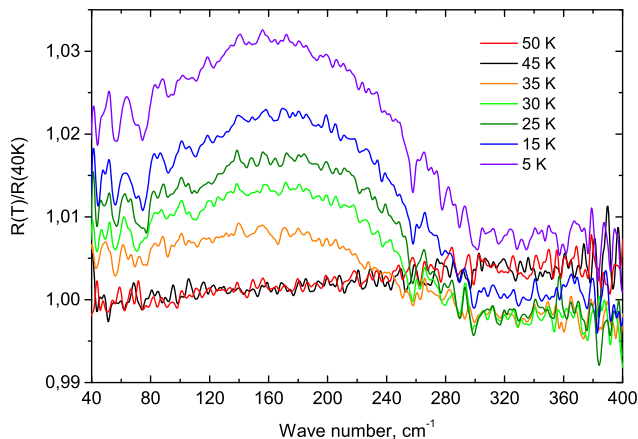


FIG. 5: $R(T)/R(40\text{ K})$ dependences of $\text{Ba}_{0.67}\text{K}_{0.33}\text{Fe}_2\text{As}_2$ measured within the temperature range $T = 5 - 50\text{ K}$.

The peak position correlates with the magnitude of the greater of the superconducting gaps [12, 33, 70–72]. The smaller gap is beyond the frequency range of our IR measurements. The kink in the normalized reflectivity at $\sim 250\text{ cm}^{-1}$ is probably due to the IR active phonon mode E_u related to the $\text{Fe}(ab)\text{-As}(-ab)$ vibrations [73]. This mode manifests itself in many AFe_2As_2 materials including $A = \text{Ca, Sr, Eu and Ba}$.

INTRINSIC MULTIPLE ANDREEV REFLECTION EFFECT (IMARE) SPECTROSCOPY

In ballistic mode, superconductor - normal metal - superconductor (SnS) contact (whose diameter $2a$ is less than the carrier mean free path l [74]) demonstrates multiple Andreev reflection effect (MARE) [75–78]. MARE manifests itself in an excess current at low bias voltages in current-voltage characteristic (CVC) of SnS contact (so called foot area). A series of dynamic conductance features called subharmonic gap structure (SGS) appears at bias voltages $V_n = 2\Delta/en$ (where n is a natural number) [75–79]. This simple formula enables to directly determine the superconducting gap value at any temperatures up to T_c [75, 77]. For the high-transparency SnS-Andreev regime (typical for our break-junction contacts), SGS exhibits a series of dips for both nodeless and nodal gap [79–81]. The coexistence of two independent superconducting gaps would cause, obviously, two SGS's in the $dI(V)/dV$ -spectrum. The k -space angular distribution of the gap value strongly affects the SGS lineshape. In case of an isotropic gap, the SGS minima are high-intensive and symmetrical, whereas a nodal gap (such as d -wave) leads to strongly suppressed and asymmetric $dI(V)/dV$ minima [79–81]. For extended s -wave nodeless symmetry, the SGS demonstrates doublet minima corresponding to

the gap extremes in the k -space [28, 80].

Experimental

For Andreev spectroscopy studies, we used a break-junction technique (for details, see [80, 82]) in order to create symmetric SnS contacts. The studied sample is precisely cracked in cryogenic environment. We cut from the single crystal a thin plate, $3 \times 1.5 \times 0.1\text{ mm}^3$. The crystal was attached to a springy holder by four In-Ga pads which insured true 4-probe connection and helped aligning the ab -plane parallel to the sample holder. After cooling down to 4.2 K, the sample holder was precisely bent, which caused cracking of the single crystal. Its deformation generates a microcrack that represents the superconductor - constriction - superconductor contact (ScS), where the constriction formally acts as insulator or normal metal. In our setup, the superconducting banks are kept touching each other and not separated to a valuable distance [80]. Taking in mind the metallic-type Ba spacers between superconducting Fe-As blocks of crystal structure, a formation of a metallic-type constriction is feasibly. The observed $I(V)$ and $dI(V)/dV$ of the break junctions are typical for high-transparent SnS-Andreev mode [75–78]. Obviously, a current flows through the break junction along the c -direction (for the details see [80]), therefore, a gap anisotropy could be barely resolved in $k_x k_y$ plane [80]. Since in our setup the microcrack is located deep in the bulk of the sample and away from current leads, the cryogenic clefts are free of Joule overheating, and adverse surface influence such as possible degradation or impurity diffusing.

In layered sample, the break-junction probe often shows also array of the SnSn-...-S-type realized in natural steps and terraces onto cryogenic clefts of layered crystal. In such arrays, an intrinsic multiple Andreev reflections effect occurs. This effect is similar to the intrinsic Josephson effect [83, 84] and was first observed in Bi cuprates [85], further in all layered superconductors ([30], for a review, see [80]). Since Andreev array consists of a sequence of m identical SnS-junctions, the SGS dips appear at positions:

$$V_n = \frac{m \times 2\Delta_i}{en}, m = 1, 2, \dots \quad (15)$$

In case of stack contacts, positions of other peculiarities caused by *bulk* properties of material also scale by a factor of m [30, 80]. In our experiment, we were able to probe tens of arrays (containing various number of junctions m) by precisely readjusting the microcrack. The latter opportunity helps one to collect a large amount of data and to check reproducibility of the *bulk* gap values and other peculiarities caused by *bulk* properties of material. The number of junctions m can be determined by

normalizing the spectrum of array to that of the single SnS-contact; after such scaling, positions of each SGS should coincide. Probing such *natural* stack contacts, one obtains information about the true bulk properties of the sample (almost unaffected by surface states which seem to be significant in Ba-122 [86] *locally*, i.e. within the contact size $a \approx 7 - 50$ nm. This feature favors accuracy increasing in the superconducting gap measurements [30].

Results

Figure 6a shows a typical current-voltage characteristic (blue line, $T = 4.2$ K) for a break-junction in nearly optimal $\text{Ba}_{0.65}\text{K}_{0.35}\text{Fe}_2\text{As}_2$ with critical temperature $T_c^{\text{local}} \approx 36$ K. The excess current at low bias voltages (foot area) manifests a formally metallic-type constriction with ballistic *c*-axis transport [75–78]. Taking the contact resistance $R \approx 15 \Omega$, the bulk in-plane resistivity of the studied crystal $\rho^{ab} \approx 0.4 \cdot 10^{-5} \Omega \cdot \text{cm}$, and using the value $\rho^{ab}l \approx 0.45 \cdot 10^{-9} \Omega \cdot \text{cm}^2$ [87], we estimate the elastic mean free path of carriers $l^{ab} \approx 1.1 \mu\text{m}$, and the contact radius $a = \sqrt{\frac{4}{3\pi} \cdot \frac{\rho^{ab}l}{R}} \approx 36$ nm. This rough estimation gives the contact dimension $2a \ll l$, which satisfies the conditions of MARE observation.

The corresponding $dI(V)/dV$ spectrum (red line in Fig. 6a) shows a set of dynamic conductance dips typical for clean classical SnS-Andreev array of 2 junctions (a natural SnSnS structure). In order to normalize $I(V)$ and $dI(V)/dV$ in Fig. 6a to those for a single SnS-junction, the voltage axis was scaled by a factor of $m = 2$. The large gap SGS starts with the clear dips at $\approx \pm 18$ mV corresponding, in accordance with the SGS expression, to $2\Delta_L/e$. The next features at $\approx \pm 11.5$ mV do not match the expected position ($\approx \pm 9$ mV) of the second subharmonic of the large gap, therefore these two dips could be interpreted as a doublet $n = 1$ feature caused by a 33 % gap anisotropy. The positions of the next pair of dynamic conductance features, $\approx \pm 9.6$ and $\approx \pm 6.4$ mV, corresponds well with those of the second subharmonic of the large gap. Note that the $n = 2$ doublet is right twice narrower than the $n = 1$ one, agreeing with the subharmonic set. To say, whether the $dI(V)/dV$ doublets are caused by the in-plane gap anisotropy in the *k*-space, or the order parameter fine splitting, one needs a further study of the dynamic conductance lineshape. In Fig. 6a, the real shape of Δ_L subharmonics is rather ambiguous since overlapped by the pronounced excess conductance. Surely, the intensity and the shape of the Δ_L dips is inconsistent with that expected for *d*-wave or fully anisotropic (nodal) *s*-wave symmetry [79, 81]; we conclude therefore that the large gap is nodeless. On the other hand, comparing the current data with those obtained earlier with Ba(K)-122 single crystals with a bit

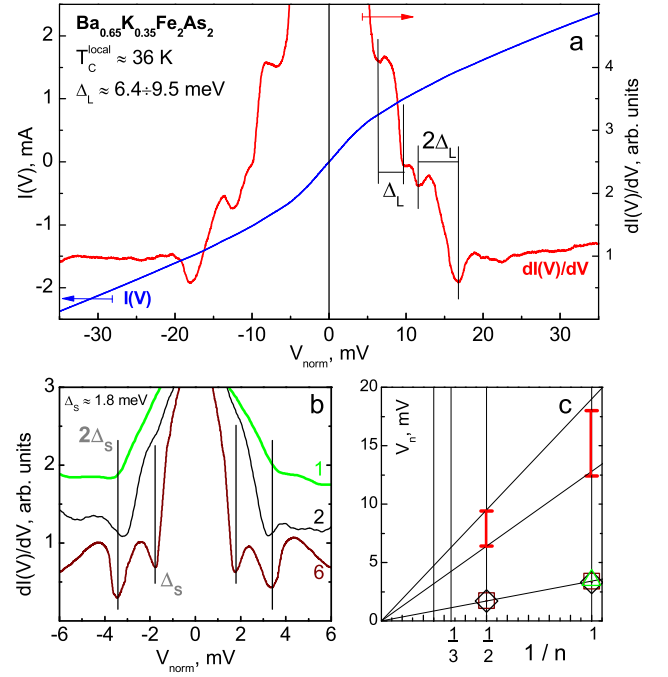


FIG. 6: a) Normalized to a single junction current-voltage characteristic (left axis) and dynamic conductance spectrum (right axis) for Andreev array in $\text{Ba}_{0.65}\text{K}_{0.35}\text{Fe}_2\text{As}_2$ with $T_c^{\text{local}} \approx 36$ K measured at $T = 4.2$ K. Black vertical lines depict the positions of subharmonic gap structure (SGS) dips, corresponding to $\Delta_L \approx 6.4\text{--}9.5$ meV (33% anisotropy in *k*-space angle distribution). b) Low-bias fragments of dynamic conductance spectra demonstrating SGS (marked with black vertical lines) of the small gap $\Delta_S \approx 1.8$ meV. The $dI(V)/dV$ of $m = 6$ and $m = 2$ contacts (lower curves) were normalized to the single SnS-junction spectrum (upper curve). Monotonic background was suppressed for clarity. c) The positions of Δ_L (vertical bars depict the gap anisotropy) and Δ_S (open symbols) subharmonics in the dynamic conductance spectra shown in a, b panels. Black lines are guidelines.

lower $T_c \approx 34$ K [46], the extended *s*-wave symmetry of the large gap is more likely.

Using Eq. (15), we directly determine the large gap edges $\Delta_L^{\text{min}} \approx 6.4$ meV, $\Delta_L^{\text{max}} \approx 9.5$ meV, and corresponding BCS ratios $2\Delta_L/k_B T_c \approx 4.1\text{--}6.1$. When trying to regard this array as corresponding to a single SnS-junction, we get the twice BCS-ratio up to 12.2 seemed too large for Ba-122; on the other hand, given $m \geq 3$, we get $2\Delta_L/k_B T_c \approx 2\text{--}3$ which is impossible for driving gap since lies below the weak-coupling limit 3.5. This simple check demonstrates a way for correct determination of the number of junctions in the array; in the case, the 2-junction structure is identified unambiguously.

Figure 6b shows low-bias fragments of dynamic conductance spectra of $m = 6$ and $m = 2$ Andreev arrays, and a single SnS junction (upper curve). The width and the outlook of the pronounced foot near zero bias is reproducible in all the curves. The monotonic

background was suppressed in order to clarify the small gap SGS. Black vertical lines in Fig. 6b mark the first feature at $V_{S1} \approx \pm 3.5$ mV and the second feature at $V_{S2} \approx \pm 1.8$ mV. These subharmonics, obviously, do not belong to the large gap SGS (see Fig. 6a), rather, they originate from a small gap $\Delta_S \approx 1.8$ meV. Unlike the Δ_L dips, the small gap peculiarities are not split and are rather symmetric, thus pointing to nearly isotropic Δ_S in k -space. Despite the fact that the three dynamic conductance spectra shown in Fig. 6b are obtained with different Ba(K)-122 samples (with the same T_c), the positions of Δ_S SGS's are reproducible. The sharpening of Andreev features with the m increasing is a representative for IMARE spectroscopy [30, 80] and evidences the bulk nature of the Δ_S order parameter.

The dependence of SGS positions V_n versus their inverse number $1/n$ shown in Fig. 6c agrees with Eq. 15 and represents straight lines crossing the origin. Two independent SGS observed in $dI(V)/dV$ spectra are caused by a presence of at least two distinct condensates with Δ_L and Δ_S order parameters.

The temperature dependences $\Delta_L(T)$ (corresponding to the positions of the outer dip of doublet-like SGS) and $\Delta_S(T)$ obtained directly are shown in Fig. 7. The dependence of the inner Δ_L extremum is an issue of further studies. The local critical temperature (corresponding to the contact area of $1 \mu\text{m}$ size transition to the normal state) $T_c^{\text{local}} \approx 36$ K is a bit lower than the bulk T_c determined with a bulk probe (see the resistive transition in Fig. 7). A single-band model (dash-dot line), obviously, is inconsistent to describe the experimental temperature dependences of the large and the small gaps. $\Delta_L(T)$ passes below the single-band BCS-like curve, whereas $\Delta_S(T)$ bends down significantly. These deviation from the single-band type are caused by a moderate interband interaction. As a result, both gaps turn to zero at common critical temperature T_c^{local} .

To approximate the experimental $\Delta_{L,S}(T)$, we used a two effective bands model based on Moskalenko and Suhl gap equations [88, 89] with a renormalized BCS-integral. The shape of gap temperature behavior depends on a set of electron-boson coupling constants $\lambda_{ij} = V_{ij}N_j$, where $i, j = L, S$, V_{ij} are matrix interaction elements, $N_{i,j}$ —normal density of states (DOS) in the corresponding bands at the Fermi level. We took the Debye energy $\hbar\omega_D = 20$ meV [90]; as fitting parameters, we used $\alpha = N_S/N_L$ ratio (hereafter “L” index is linked with the driving bands), and the relation between intra- and interband coupling $\beta = \sqrt{V_L V_S}/V_{LS}$, the fitting is detailed in [27, 91]. Theoretical $\Delta_{L,S}(T)$ shown by solid lines agree well with the experimental dependences, therefore, the simple two effective bands model is applicable to describe the IMARE data. The observed $\Delta_{L,S}(T)$ are typical for a strong intraband coupling in the driving bands. The large gap BCS-ratio far exceeding the weak-coupling BCS limit, also favors the latter statement. In contrast,

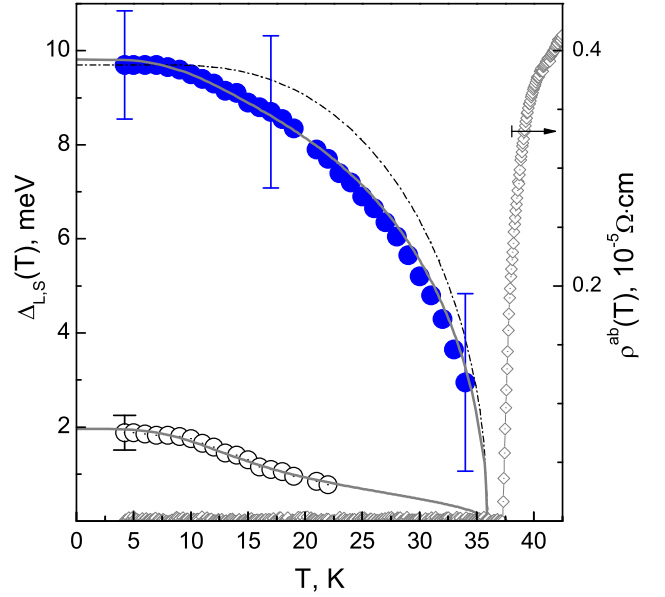


FIG. 7: Temperature dependences of the large gap (blue solid circles) and the small gap (open circles) in $\text{Ba}_{0.65}\text{K}_{0.35}\text{Fe}_2\text{As}_2$. Single-band BCS-like curve (dash-dot line) and bulk resistive transition (rhombs) are shown for comparison.

the Moskalenko-Suhl fit proves a weak-pairing superconductivity in the driven bands solely. In a hypothetical case of zero interband interaction ($V_{LS} = 0$), we estimate $2\Delta_S/k_B T_c^S \approx 3.5$ (T_c^S is the eigen critical temperature of the bands where the small gap is developed).

Taking zero Coulomb pseudopotentials $\mu^* = 0$ suggested, for example, in [92, 93], we get $\lambda_{LL} = 0.59$, $\lambda_{SS} = 0.28$, $\lambda_{LS} = 0.24$, $\lambda_{SL} = 0.02$ leading to extremely large DOS ratio $\alpha \sim 12$, and intra- to interband coupling ratio $\beta \sim 6$, which is impossible for the so-called s^\pm scenario proposed in [92, 93]. When accepting a moderate nonzero Coulomb repulsion $\mu^* = 0.2$, we roughly estimate $\lambda_{LL} = 0.73$, $\lambda_{SS} = 0.43$, $\lambda_{LS} = 0.4$, $\lambda_{SL} = 0.13$, seemed more realistic. In the latter case, $\alpha \approx 3$, whereas the intraband coupling is 2.4 times stronger than interband one.

DISCUSSION

The gap values obtained using the four complementary techniques are summarized in the Table 1. H_{c1} and $C(T)$ probe bulk properties, IR spectroscopy provides information about crystal subsurface layer, whereas IMARE is a direct local probe of the bulk order parameter. Our experimental data $C_{el}(T)$ and $H_{c1}(T)$ may be well fitted with the two isotropic nodeless gaps. The Andreev spectroscopy data points at two distinct gaps, the anisotropic large gap and isotropic small gap. All the data converge on the absence of nodes for both gaps. For the large gap, we report the BCS ratio $2\Delta_L/k_B T_c = 6.1 - 7.2$ exceed-

TABLE I: The superconducting transition temperature T_c , and the superconducting gap properties extracted from data obtained for $\text{Ba}_{1-x}\text{K}_x\text{Fe}_2\text{As}_2$ by different methods.

Compounds	$T_c(\text{K})$	Nodes, anisotropy	$\Delta_L(\text{meV})$ ($2\Delta_L/k_B T_c$)	weight $_L$	$\Delta_S(\text{meV})$ ($2\Delta_S/k_B T_c$)	weight $_S$	Δ_L/Δ_S	Technique	Ref.
$x = 0.33$	36.5	no	11.0 ± 0.5 (6.9 ± 0.3)	0.46	2.0 ± 0.3 (1.2 ± 0.2)	0.54	5.5 ± 0.3	magnetization	this work
$x = 0.33$	36.5	no	11.3 ± 0.3 (7.2 ± 0.2)	0.42	2.5 ± 0.2 (1.6 ± 0.1)	0.58	4.52 ± 0.3	specific heat	this work
$x = 0.33$	36.5	–	9.9 ± 1 (6.3 ± 0.6)	–	–	–	–	IR normalized	this work
$x = 0.35$	36 ± 1	no, $\approx 33\%$	$\Delta_L^{\min} = 6.4 \pm 0.7,$ $\Delta_L^{\max} = 9.5 \pm 1.0$ ($4 - 6 \pm 0.6$)	–	1.8 ± 0.3 (1.1 ± 0.2)	–	$3.6 - 5.3$	break-junction	this work
$x = 0.4$	35.8	no	8.8 ± 0.3 (5.7 ± 0.2)	0.3	2.2 ± 0.2 (1.4 ± 0.1)	0.7	4 ± 0.3	magnetization	[19]
$x = 0.32$	38.5	no	11 (6.6)	0.5	3.5 (2.2)	0.5	3.14	specific heat	[12]
$x = 0.35$	34 ± 3	no, $\approx 30\%$	5.8–8.0 ($4 - 5.5$)	–	1.7 ± 0.3 (1.2 ± 0.2)	–	4.4 ± 0.3	break-junction	[46]
$x = 0.32$	38.5	no	10 (6)	–	3.7 (2.2)	–	2.7	IR	[71]
$x = 0.4$	38	no	10 ± 1 (6.1 ± 0.6)	–	$(3 - 5.5) \pm 1$ ($1.8 - 3.4 \pm 0.6$)	–		ARPES	[72]

ing the BCS-limit. This slight variation could be caused by several reasons, such as (a) out-of-plane anisotropy of the order parameter discussed in [94], (b) a complex and nontrivial in-plane angle distribution of the large gap in the k -space, (c) a possible presence of a large gap splitting, (c) a surface sensitivity of superconducting properties, (d) a significant contribution of high-energy ($\omega > \Delta$) pairs with $\text{Re}[\Delta(\omega)] > \Delta_{exp}$ (where Δ_{exp} is a gap edge of the Eliashberg function) accounted in bulk probes. As for the small gap, the determined values give $2\Delta_S/k_B T_c = 1.2 - 1.6$ which lies well below the 3.5 limit and point to a nonzero interaction between the condensates.

It is noteworthy that our extracted gap values are comparable with the two-band s -wave fit, $\Delta_{1,2}(0) = 2$ and 8.9 meV, reported for $\text{Ba}_{0.6}\text{K}_{0.4}\text{Fe}_2\text{As}_2$ in [19] and $\Delta_{1,2}(0) = 3.5$ and 11 meV in [12]. The value of the gap amplitudes obtained for this material scales relatively well with its T_c in light of the recent results for the FeBS [46, 95].

It is important to note that ARPES studies also report two s -wave nodeless gaps of 2.3 and 7.8 meV for the outer and the inner Fermi surface sheets, respectively [96]. In fact, ARPES results hint towards the conclusion about strong dependence of the gap value on orbital character of the bands forming the corresponding Fermi surfaces: the larger gap appears on d_{xz}/d_{yz} bands [97]. Very recently, and based on a multi-band

Eliashberg analysis, for $\text{Ca}_{0.32}\text{Na}_{0.68}\text{Fe}_2\text{As}_2$ the superconducting electronic specific heat was shown to be described by a three-band model with an unconventional s_{\pm} pairing symmetry with gap magnitudes of approximately 2.35, 7.48, and formally -7.50 meV [21]. It has been well demonstrated that the model based on Eliashberg equations is a simplified model of the real four bands model taking into account the similarities between the two 3D Fermi sheets and between the two 2D Fermi sheets. Based on them for the determination of T_c and for the gap functions there can be considered only a distinct gap for every 2D, and respectively 3D sets of bands [98]. In fact, the Eliashberg equations may be solved in two ways. The first way is to solve the equations which contain dependences of real frequency, and the second one – to solve this equations on the imaginary axis, summing on Matsubara frequencies [99]. Thus, the uncertainty in the number of SC condensates to be involved into the data processing affects the parameters extracted from the experiment. In this work we used the simple α -model that is not self-consistent, but is often used by experimentalists for fitting their thermodynamic data that deviate from the BCS predictions and for quantifying those deviations [100]. From the temperature dependence of the lower critical field data or specific heat data alone it is difficult to be sure whether one, two or three bands can describe well our investigated system, since in the case of multiband superconductivity low-energy quasiparticle

excitations can be always explained by the contribution from an electron group with a small gap.

By complementing presented data as well as the data on $\text{BaFe}_{1.9}\text{Ni}_{0.1}\text{As}_2$ single crystals ($T_c \approx 19$ K) [101] obtained with MARE spectroscopy with the existing ARPES results [15, 20, 72, 96], one could make conclusion on ab-plane anisotropy of the large order parameter Δ_L . Comparing the H_{c1} , $C(T)$, and IMARE data, the two-band model seems to be sufficient to describe the experimental temperature dependences of superconducting parameters.

CONCLUSIONS

Using four complementary experimental techniques, we studied single crystals of the 122 family, nearly optimally doped $\text{Ba}_{1-x}\text{K}_x\text{Fe}_2\text{As}_2$, and obtained consistent data on the structure of the superconducting order parameter. Our data extracted from (i) temperature dependence of lower critical field, and (ii) temperature dependence of the specific heat, are inconsistent with a single s -wave order parameter but is rather in favor of the presence of two gaps without nodes. Our infrared reflection spectra supports the magnitude of the large gap, obtained from SH and lower critical field data, and its nodeless character. The IMARE spectroscopy data, obtained on SnS -Andreev arrays, refine the conclusions on the two nodeless gaps: the large gap, $\Delta_L = 6.4 - 9.5$ meV with extended s -wave symmetry and anisotropy in the k -space not less than $\approx 30\%$, and the small gap, $\Delta_S = 1.8 \pm 0.3$ meV. The BCS-ratio for the the upper extremum of the large gap is $2\Delta_L/k_B T_c \approx 6.1 - 7.2$. All our data clearly show that the superconducting energy gaps in nearly optimally doped $\text{Ba}_{1-x}\text{K}_x\text{Fe}_2\text{As}_2$ are nodeless. In addition, the obtained gaps are consistent with those determined from ARPES measurements.

ACKNOWLEDGEMENTS

This work is supported by the Russian Science Foundation (16-12-10507). Magnetic measurements were carried out with the support of the Russian Foundation for Basic Research (16-32-00663). M.A. acknowledges funding by DFG in the project MO 3014/1-1. YuAA acknowledges the support of the Competitiveness Program of NRNU MEPhI. Authors also acknowledge the Shared Facility Center at LPI for using their equipment.

* Electronic address: avmuratov@mail.ru

[1] J. Paglione and R. L. Greene, Nat. Phys. **6**, 645 (2010).
 [2] G. R. Stewart, Rev. Mod. Phys. **83**, 1589 (2011).

- [3] I. R. Fisher, L. Degiorgi, and Z. X. Shen, Rep. Prog. Phys. **74**, 124506 (2011).
 [4] P. J. Hirschfeld, M. M. Korshunov, and I. I. Mazin, Rep. Prog. Phys. **74**, 124508 (2011).
 [5] D. N. Basov and A. V. Chubukov, Nat. Phys. **7**, 272 (2011).
 [6] P. Dai, J. Hu, and E. Dagotto, Nat. Phys. **8**, 709 (2012).
 [7] M. Rotter, M. Tegel and D. Johrendt, Phys. Rev. Lett. **101**, 107006(2008). arXiv:0805.4630v1(2008).
 [8] L. X. Yang, et al. Phys. Rev. Lett. **102**, 107002 (2009). arXiv: 0806.2627
 [9] X. F. Wang, T. Wu, G. Wu, H. Chen, Y. L. Xie, J. J. Ying, Y. J. Yan, R. H. Liu, X. H. Chen, Phys. Rev. Lett. **102**, 117005 (2009). arXiv:0806.2452v2
 [10] G. Wu, R. H. Liu, H. Chen, Y. J. Yan, T. Wu, Y. L. Xie, J. J. Ying, X. F. Wang, D. F. Fang, X. H. Chen. Europhys. Lett. **84**, 27010(2008).
 [11] H. Chen, Y. Ren, Y. Qiu, Wei Bao, R. H. Liu, G. Wu, T. Wu, Y. L. Xie, X. F. Wang, Q. Huang, X. H. Chen, Europhys. Lett. **85**, 17006 (2009).
 [12] P. Popovich, A. V. Boris, O. V. Dolgov, A. A. Golubov, D. L. Sun, C. T. Lin, R. K. Kremer, and B. Keimer, Phys. Rev. Lett. **105**, 027003 (2010).
 [13] V. B. Zabolotnyy, D. S. Inosov, D. V. Evtushinsky, A. Koitzsch, A. A. Kordyuk, G. L. Sun, J. T. Park, D. Haug, V. Hinkov, A. V. Boris, C. T. Lin, M. Knupfer, A. N. Yaresko, B. Buechner, A. Varykhalov, R. Follath, S. V. Borisenko, , Nature Lett. **457**, 569 (2009)
 [14] Y. Zhang, Z. R. Ye, Q. Q. Ge et al. Nature Phys. **8**, 371 (2012)
 [15] H. Ding, P. Richard, K. Nakayama, K. Sugawara, T. Arakane, Y. Sekiba, A. Takayama, S. Souma, T. Sato, T. Takahashi, Europhys. Lett. **83**, 47001 (2008).
 [16] Y. Zhang, L. X. Yang, F. Chen, B. Zhou, X. F. Wang, X. H. Chen, M. Arita, K. Shimada, H. Namatame, M. Taniguchi, J. P. Hu, B. P. Xie, and D. L. Feng, Phys. Rev. Lett., **105**, 117003 (2010)
 [17] G. Mu, H. Luo, Z. Wang, L. Shan, C. Ren, and H.-H. Wen, Phys. Rev. B **79**, 174501 (2009).
 [18] Ch. Kant, J. Deisenhofer, A. Guenther, F. Schrettle, and A. Loidl, M. Rotter, and D. Johrendt, Phys. Rev. B **81**, 014529 (2010).
 [19] Cong Ren, Zhao-Sheng Wang, Hui-Qian Luo, Huan Yang, Lei Shan, and Hai-Hu Wen, , Phys. Rev. Lett. **101**, 257006 (2008).
 [20] R. Khasanov, D. V. Evtushinsky, A. Amato, H.-H. Klauss, H. Luetkens, Ch. Niedermayer, B. Bchner, G. L. Sun, C. T. Lin, J. T. Park, D. S. Inosov, and V. Hinkov, Phys. Rev. Lett. **102**, 187005 (2009)
 [21] S. Johnston, M. Abdel-Hafiez, L. Harnagea, V. Grinenko, D. Bombor, Y. Krupskaya, C. Hess, S. Wurmehl, A. U. B. Wolter, B. Büchner, H. Rosner, and S.-L. Drechsler, Phys. Rev. B **89**, 134507 (2014).
 [22] A. K. Pramanik, M. Abdel-Hafiez, S. Aswartham, A. U. B. Wolter, S. Wurmehl, V. Kataev, and B. Büchner Phys. Rev. B **84**, 064525 (2011).
 [23] F. Hardy, R. Eder, M. Jackson, *et al.*, J. Phys. Soc. Jpn. **83**, 014711 (2014).
 [24] H. Padamsee, J. E. Neighbor, and C. A. Shifman, J. Low Temp. Phys. **12**, 387 (1973).
 [25] F. Bouquet, Y. Wang, R.A. , Europhys. Lett. **56** (6), 856 (2001).
 [26] S. A. Kuzmichev, T. E. Shanygina, S. N. Tchesnokov, S. I. Krasnosvobodtsev, Sol. State Commun. **152**, 119

- (2012)
- [27] S. A. Kuzmichev, T. E. Kuzmicheva, S. N. Tchesnokov, JETP Lett. **99**, 295 (2014).
 - [28] S. A. Kuzmichev, T. E. Kuzmicheva, A. I. Boltalin, and I. V. Morozov, JETP Lett. **98**, 722 (2013).
 - [29] T. E. Kuzmicheva, S. A. Kuzmichev, N. D. Zhigadlo, JETP Lett. **99**, 136 (2014).
 - [30] T.E. Kuzmicheva, S.A. Kuzmichev, M.G. Mikheev, Ya.G. Ponomarev, S.N. Tchesnokov, Yu.F. Eltsev, V.M. Pudalov, K.S. Pervakov, A.V. Sadakov, A.S. Usoltsev, E.P. Khlybov, L.F. Kulikova, Europhysics Letters **102**, 67006 (2013)
 - [31] T. E. Shanygina, S. A. Kuzmichev, M. G. Mikheev, Y.G. Ponomarev, S.N. Tchesnokov, Y.F. Eltsev, V.M. Pudalov, A.V. Sadakov, A.S. Usoltsev, J. Supercond. Nov. Magn. **26**, 2661 (2013).
 - [32] Lin Zhao, Haiyun Liu, Wentao Zhang, Jianqiao Meng, Xiaowen Jia, Guodong Liu, Xiaoli Dong, G. F. Chen, J. L. Luo, N. L. Wang, Guiling Wang, Yong Zhou, Yong Zhu, Xiaoyang Wang, Zhongxian Zhao, Zuyan Xu, Chuangtian Chen, X. J. Zhou, Chin. Phys. Lett. **25**, 4402 (2008).
 - [33] Lei Shan, Yong-Lei Wang, Jing Gong, Bing Shen, Yan Huang, Huan Yang, Cong Ren, and Hai-Hu Wen, Phys. Rev. B **83**, 060510 (2011).
 - [34] R. Thomale, C. Platt, W. Hanke, and B. A. Bernevig, Phys. Rev. Lett. **106**, 187003 (2011).
 - [35] S. Maiti and A. V. Chubukov, Phys. Rev. B **82**, 214515 (2010).
 - [36] C. Platt, R. Thomale, and W. Hanke, Phys. Rev. B **84**, 235121 (2011).
 - [37] T. A. Maier, S. Graser, D. J. Scalapino, and P. J. Hirschfeld, Phys. Rev. B **79**, 224510 (2009).
 - [38] A. F. Kemper, T. A. Maier, S. Graser, H.-P. Cheng, P. J. Hirschfeld, and D. J. Scalapino, New J. Phys. **12**, 073030 (2010).
 - [39] A.V. Chubukov, D.V. Efremov, and I. Eremin, Phys. Rev. B **78**, 134512 (2008).
 - [40] J.-P. Castellan, S. Rosenkranz, E. A. Goremychkin, D. Y. Chung, I. S. Todorov, M. G. Kanatzidis, I. Eremin, J. Knolle, A. V. Chubukov, S. Maiti, M. R. Norman, F. Weber, H. Claus, T. Guidi, R. I. Bewley, and R. Osborn, Phys. Rev. Lett. **107**, 177003 (2011).
 - [41] D.V. Efremov, M.M.Korshunov, O.V. Dolgov, et al., Phys. Rev. B **84**, 180512 (2011)
 - [42] K. Nakayama et al., Phys. Rev. B **83**, 020501 (2011).
 - [43] K. Terashima et al., Proc. Natl. Acad. Sci. USA **106**, 7330 (2009).
 - [44] J.-Ph. Reid, M. A. Tanatar, X. G. Luo, H. Shakeripour, et al. L. Taillefer, Phys. Rev. B **82**, 064501 (2010); M. A. Tanatar, J.-Ph. Reid, H. Shakeripour, et al. Phys. Rev. Lett. **104**, 067002 (2010).
 - [45] H. Kim, M. A. Tanatar, Y. J. Song, Y. S. Kwon, and R. Prozorov, Phys. Rev. B **83**, 100502 (2011).
 - [46] M. Abdel-Hafiez, P. J. Pereira, S. A. Kuzmichev, T. E. Kuzmicheva, V. M. Pudalov, L. Harnagea, A. A. Kordyuk, A. V. Silhanek, V. V. Moshchalkov, B. Shen, Hai-Hu Wen, A. N. Vasiliev, and Xiao-Jia Chen, Phys. Rev. B **90**, 054524 (2014).
 - [47] I.S. Blokhin, S. Yu. Gavrilkin, B. P. Gorshunov, et al., ZhETF **148**(5), 976 (2015). [JETP **121**(5) (2015)]. V.M. Pudalov, T.E. Kuzmicheva, S.A. Kuzmichev, A.V. Muratov, Yu.A. Aleshenko, A.V. Sadakov, K.V.Mitsen, O.M.Ivanenko, S.Yu. Gavrilkin, I.S. Blokhin, A.A. Kordyuk, M. Abdel-Hafiez, in: Proceed. Ugo Fano Symposium, RICMAS, Rome (2015).
 - [48] M. B. Schilling, A. Baumgartner, B. Gorshunov, E. S. Zhukova, V. A. Dravin, K. V. Mitsen, D. V. Efremov, O. V. Dolgov, K. Iida, M. Dressel, and S. Zapf, PRB **93**, 174515 (2016).
 - [49] A. V. Burmistrova, I. A. Devyatov, Alexander A. Golubov, Keiji Yada, Yukio Tanaka, M. Tortello, R. S. Gonnelli, V. A. Stepanov, Xiaxin Ding, Hai-Hu Wen, and L. H. Greene, PRB **91**, 214501 (2015)
 - [50] L. Shan, Y. L. Wang, B. Shen, B. Zeng, Y. Huang, A. Li, D. Wang, H. Yang, C. Ren, Q. H. Wang, Z. H. Pan, and H. H. Wen, Nature Physics **7**, 325 (2010).
 - [51] H. Q. Luo, Z. S. Wang, H. Yang, P. Cheng, X. Y. Zhu, and H. H. Wen, Supercond. Sci. Technol. **21**, 125014 (2008).
 - [52] S. Avci, O. Chmaissem, D. Y. Chung, et al., Phys. Rev. B **85**, 184507 (2012).
 - [53] T E Kuzmicheva, S A Kuzmichev, M G Mikheev, Ya G Ponomarev, S N Tchesnokov, V M Pudalov, E P Khlybov, N D Zhigadlo, Phys.-Uspekhi **57**(8), 819 (2014).
 - [54] R. Prozorov and V. G. Kogan, Reports on Progress in Physics **74**, 124505 (2011).
 - [55] M. Abdel-Hafiez, J. Ge, A. N. Vasiliev, D. A. Chareev, J. Van de Vondel, V. V. Moshchalkov, and A. V. Silhanek, Phys. Rev. B **88**, 174512 (2013).
 - [56] E. H. Brandt PRB **60**, 11939 (1999).
 - [57] A. Carrington and F. Manzano, Physica C (Amsterdam) **385**, 205 (2003).
 - [58] H. G. Luo and T. Xiang, Phys. Rev. Lett. **94**, 027001(2005).
 - [59] J.W. Stout and E. Catalano, J. Chem. Phys. **23**, 2013 (1995).
 - [60] F. Hardy, T.Wolf, R.A. Fisher et al., PRB **81**, 060501(R) (2010).
 - [61] M. Abdel-Hafiez, Y. Zhang, Z. He, PRB **91**, 024510 (2015).
 - [62] P. Popovich, A.V. Boris, O.V. Dolgov, Phys. Rev. Lett. **105**, 027003 (2010). Supplementary online material
 - [63] B. Muhlschlegel, Z. Phys, **155** (1959) 313.
 - [64] D.N. Basov and T. Timusk, Rev. Mod. Phys. **77**, 721 (2005).
 - [65] G. Burns, Solid State Physics (Academic Press), Boston, 1990.
 - [66] D.C. Mattis and J. Bardeen, Phys. Rev. **111**, 412 (1958).
 - [67] M. Tinkham, Introduction to Superconductivity (McGraw-Hill, New York, 1975).
 - [68] W. Zimmermann, E.H. Brandt, M. Bauer, et al., Physica C **183**, 99 (1991).
 - [69] L.H. Palmer and M. Tinkham, Phys. Rev. **165**, 588 (1968).
 - [70] D.V. Evtushinsky, D.S. Inosov, V.B. Zabolotnyy, et al., Phys Rev. B **79**, 054517 (2009).
 - [71] A. Charnukha, O.V. Dolgov, A.A. Golubov, et al., Phys Rev. B **84**, 174511 (2011).
 - [72] D.V. Evtushinsky, V.B. Zabolotnyy, T.K. Kim, Phys Rev. B **89**, 064514 (2014).
 - [73] A.A. Schafgans, B.C. Pursley, A.D. LaForge, et al., Phys Rev. B **84**, 052501 (2011).
 - [74] Yu. V. Sharvin, Sov. Phys. JETP **21**, 655 (1965).
 - [75] M. Octavio, M. Tinkham, G. E. Blonder, and T. M. Klapwijk, Phys. Rev. B **27**, 6739 (1983).
 - [76] G. B. Arnold, J. Low Temp. Phys. **68**, 1 (1987).

- [77] R. K  mmel, U. Gunsenheimer, and R. Nikolsky, Phys. Rev. B **42**, 3992 (1990).
- [78] D. Averin and A. Bardas, Phys. Rev. Lett. **75**, 1831 (1995)
- [79] T. P. Devereaux and P. Fulde, Phys. Rev. B **47**, 14638 (1993).
- [80] S.A. Kuzmichev, T.E. Kuzmicheva, Low. Temp. Phys **42**, 1008 (2016).
- [81] A. Poenicke, J. C. Cuevas, and M. Fogelstroem, Phys. Rev. B **65**, 220510(R) (2002).
- [82] J. Moreland and J. W. Ekin, J. Appl. Phys. **58**, 3888 (1985).
- [83] B. A. Aminov, L. I. Leonyuk, T. E. Oskina, *et al.*, Adv. Supercond. V, 1037 (1993).
- [84] H. Nakamura, *et al.* J. Phys. Soc. Jpn. **78**, 123712 (2009).
- [85] Ya. G. Ponomarev, *et al.*, Inst. Phys. Conf. Ser. **167**, 241 (2000).
- [86] E. van Heumen, J. Vuorinen, K. Koepernik, *et al.*, Phys. Rev. Lett. **106**, 027002 (2011).
- [87] V. N. Zverev, A. V. Korobenko, G. L. Sun, C. T. Lin, and A. V. Boris, JETP Lett. **90**, 130 (2009).
- [88] V.A. Moskalenko, Fiz. Met. Metall. **8**, 503 (1959); Sov. Phys. Usp. **17**, 450 (1974).
- [89] H. Suhl, B. T. Matthias, L. R. Walker, *et al.*, Phys. Rev. Lett. **12**, 552, (1959).
- [90] L. Rettig, R. Cortes, H. S. Jeevan, P. Gegenwart, T. Wolf, J. Fink and U. Bovensiepen, New J. Phys. **15**, 083023 (2013).
- [91] S.A. Kuzmichev, T.E. Kuzmicheva, S.N. Tchesnokov, V.M. Pudalov, A.N. Vasiliev, J. Supercond. Novel Magn. **29**, 1111 (2016).
- [92] S. Maiti, A.V. Chubukov, Phys. Rev. B **87**, 144511 (2013).
- [93] I.I. Mazin, J. Schmalian, Physica C **469**, 614 (2009).
- [94] T. Saito, S. Onari, and H. Kontani, Phys. Rev. B **88**, 045115 (2013).
- [95] Ya.G. Ponomarev, *et al.* J. Supercond. Novel Magn. **26**, 2867 (2013)
- [96] D. V. Evtushinsky, V. B. Zabolotnyy, L. Harnagea, A. N. Yaresko, S. Thirupathaiah, A. A. Kordyuk, J. Maletz, S. Aswartham, S. Wurmehl, E. Rienks, R. Follath, B. B  chner, and S. V. Borisenko, Phys. Rev. B **87**, 094501 (2013).
- [97] A. A. Kordyuk, Low Temp. Phys. **38**, 888 (2012).
- [98] O. V. Dolgov, R. K. Kremer, J. Kortus, A. A. Golubov, S. V. Shulga, Phys. Rev. B **72**, 024504 (2005).
- [99] D. J. Scalapino, J. R. Schrieffer, J. W. Wilkins, Phys. Rev. **148**, 263 (1966).
- [100] D. C. Johnston, Supercond. Sci. Technol. **26**, 115011 (2013).
- [101] T.E. Kuzmicheva, V.A. Vlasenko, S.Yu. Gavrilkin, S.A. Kuzmichev, K.S. Pervakov, I.V. Roshchina, V.M. Pudalov, J. Supercond. Novel Magn. **29**, 3059 (2016).

APPENDIX 1

Data processing protocol

As mentioned in the main text, the noise level in our $M(H)$ measurements was rather high, $3 - 5 \times 10^{-5}$ emu with the signal of the order of 10^{-2} emu. We firstly investigated the possibility of determination H_{c1} using the conventional method [46, 55]. For this purpose we model the typical $M(H)$ dependence using a piecewise analytical formulae. We break the range of measurements in two regions. In the low-field region we model the $M(H)$ data with a linear model dependence, whereas above a certain field H_0 – with a parabolic one. The parameters for both linear and non-linear parts are fitted to the measured $M(H)$ data; the step size for the model dependences was chosen 0.5 Oe. We further add a random signal within a chosen noise level to each data point of the model $M(H)$ dependence, and consider how this noise affects the correlation coefficient R , calculated by the conventional method [46, 55], and also the extracted H_{c1} value.

It appears that the correlation coefficient calculated for the noise level about 10^{-6} emu coincides with that calculated in Ref. [46]. Particularly, it exhibits a plateau below H_{c1} . By taking the field value where R starts sharply decreasing we obtain the H_{c1} value that also coincides with the H_0 parameter of the model. The inset to Fig. 8a shows a typical correlation coefficient $R(H)$ calculated for the noise level 10^{-6} emu. This dependence has a weak maximum at $H = 16$ Oe, which is only by 6% higher than the parameter $H_0 = 15$ Oe included in the model.

However, as noise increases, the $R(H)$ dependence changes drastically: the maximum becomes more clearly pronounced and its departure from H_0 increases. Figure 8a shows the correlation coefficient R calculated for the model $M(H)$ dependence with a $50\times$ bigger noise level, 5×10^{-5} (typical for the experiment), and for $H_0 = 15$ Oe. Instead of plateau, $R(H)$ here exhibits a maximum at ≈ 25 Oe which is essentially higher than the given H_0 value.

In order to overcome the problem of extraction the H_{c1} value in the presence of noise, we have modified the above algorithm of Refs. [46, 55]. In the modified method we expand the trapped magnetization M as $M(H) \propto (H - H_{c1})^2$ in the vicinity of H_{c1} . Correspondingly, the magnetization may be written as follows:

$$\begin{aligned} M(H) &= aH + b & \text{for } H < H^* \\ M(H) &= aH + b + c(H - H^*)^2 & \text{for } H > H^*. \end{aligned} \quad (16)$$

For every running data point H_i we take $H^* = H_i$ and find the best fitting of the experimental data with the model curve Eq. (16), using a, b and c as fitting parameters.

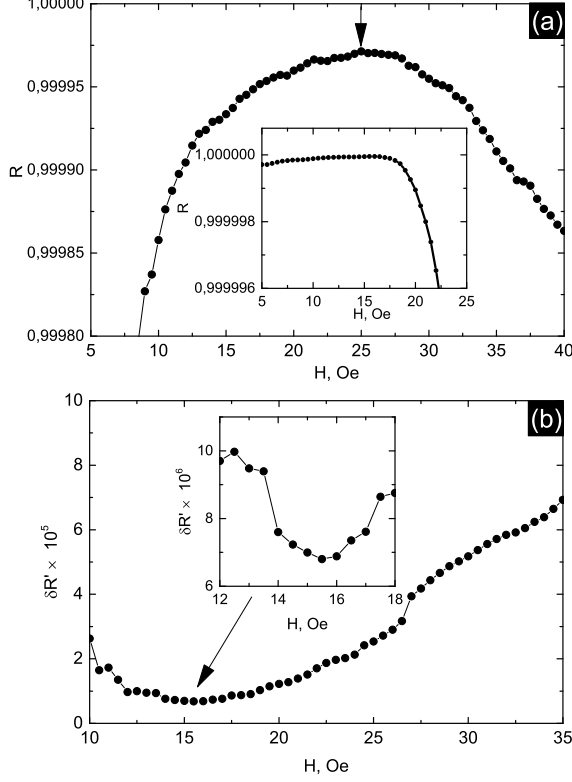


FIG. 8: (a) Correlation coefficient R calculated for model data with noise level about 5×10^{-5} emu by method used in [46, 55]. Inset: correlation coefficient R calculated for model data with noise level 10^{-6} emu. (b) Deviation of the correlation index from unity $\delta R' = 1 - R'$ versus H calculated by the modified method for the same model data.

ters (the parameter b corresponds to an insignificant, an order of 10^{-4} emu, possible residual zero field magnetization $M(H=0)$). For every $H^* = H_i$ we calculate the correlation index (coefficient of determination) as follows:

$$R'(H) = \sqrt{1 - \frac{\sum (M_{\text{exper}}(H) - M_{\text{fit}}(H))^2}{\sum (M_{\text{exper}}(H) - \bar{M})^2}}. \quad (17)$$

Here M_{fit} is the magnetization calculated within the model Eq. (16) for the given set of parameters a_i, b_i and c_i which are determined at point H_i , and \bar{M} is the av-

eraged magnetization value. The model Eq. (16) is expected to give the best fit of the experimental data at the $H_i = H_{c1}$, therefore we interpret the R' maximum point as H_{c1} .

Figure 8 b shows the deviation from unity of correlation index calculated using the modified method for the same model function $M(H)$ as that used above for calculations of R in Fig. 8 a, and for the same noise level 5×10^{-5} emu. This dependence has a maximum at $H = 15.5$ Oe that

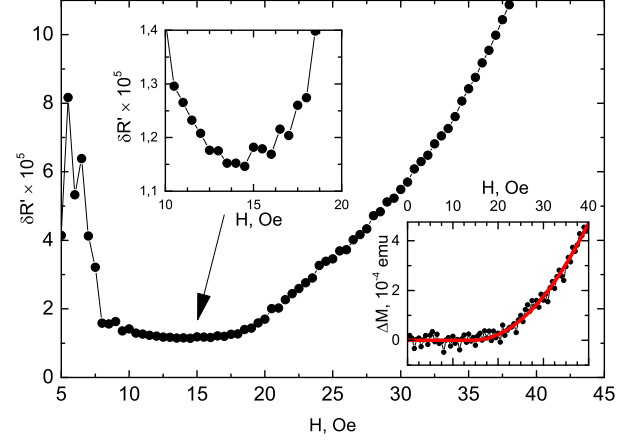


FIG. 9: Deviation from unity of the correlation index $\delta R' = 1 - R'(H)$ calculated by the modified method for the data taken at $T = 15$ K. The upper inset shows the $\delta R'(H)$ dependence near its minimum. The lower inset shows deviation of the measured $M(H)$ data from the linear $M(H)$ dependence.

agrees with $H_0 = 15$ Oe used in the model $M(H)$. By random varying the magnetization within the the same noise level we found that the maximum of R' (and therefore H_{c1}) varies within 2 Oe; we consider this as the estimate of the uncertainty of H_{c1} .

Figure 9 shows the deviation from unity of correlation index $\delta R' = 1 - R'$, versus H calculated from our experimental $M(H)$ data measured at $T = 15$ K. The upper inset shows this dependence near it's minimum. This minimum is taken as the best estimate of H_{c1} . The lower inset shows deviation of the experimental $M(H)$ data from the best linear fit calculated with parameters a_i and b_i defined for the point of maximum $R'(H_i)$. The high fit quality demonstrates the applicability of the model Eq. (16) to the experimental data.